[1]Spin-Echo Resolved Grazing Incidence Scattering (SERGIS) of cold neutrons

G.P. Felcher*[a], S.G.E. te Velthuis[a], J. Major[b], H. Dosch[b], C. Anderson[b], K. Habicht[c], and T. Keller[d]
[a]Argonne National Laboratory; [b]Max-Planck-Institut für Metallforschung Stuttgart; [c]Hahn-Meitner-Institut Berlin; [d]Max-Planck-Institut für Festkörperphysik, Stuttgart

ABSTRACT

The conceptual design of a new instrument is presented, which makes use of the spin echo technique to analyze the scattering angle of neutrons impinging upon a rough or corrugated surface at grazing incidence. In a grazing incidence geometry the roughness of the surface and of submersed interfaces give rise to a neutron scattering pattern at angles well resolved from that of specular reflection for corrugation lengths up to several microns, but only in the plane of specular reflection. In contrast, scattering caused by corrugations of comparable length perpendicular to the reflection plane is limited to angles that can be separated only with an extreme tightening of the instrumental resolution. However this scattering can be well resolved by spin-echo methods for polarized neutrons. Results from scattering in and out of the reflection plane provide complementary information on the structure of the roughness and its location in a system with complex layering. This spin-echo technique may also distinguish static from time-dependent roughness.

Keywords: neutron reflectivity, spin-echo

1. INTRODUCTION

The specular reflectometry of both X-rays and neutrons has been developed in the past two decades to measure chemical depth profiles in thin films. If the films are perfectly flat and laterally homogenous those radiations are reflected solely at an exit angle θ_f equal to the angle of incidence θ_i. The intensity of the reflected beam is a function of the momentum transfer of the radiation, $q_z = 4\pi\sin\theta/\lambda$, where λ the radiation wavelength. The reflectivity is an optical transform of the chemical depth profile. For instance, if the profile consists of a periodic layering, the reflection pattern is composed of Bragg reflections. However, since the number of layers is finite, the Bragg reflection lines are not infinitely sharp, and finite intensity is reflected at all angles. Fig. 1 shows reflectivity patterns as obtained by X-rays and neutrons, together with the chemical depth profiles that have been reconstructed[1] from them. It can be seen that the characteristic lengths measured by reflectivity are much longer than those obtained in conventional diffraction. Correspondingly, the field of q_z observed is quite restricted: since the wavelengths used are of the order of a few Ångstroms, the measurements need to be carried out at small angles (from a fraction of to a few degrees). In such conditions refractive effects become important, and below a characteristic value of q total reflection takes place. Specular reflectivity gives the one dimensional profile of a film, whose thickness can be of a few, or up to a few thousand Ångstroms[2]. Since in practice hardly any film is laterally homogeneous, specular reflectivity gives information only on the lateral average of the films. The fluctuations of chemistry or density within the plane of the film instead give rise to off-specular scattering of the beam sent at grazing incidence[3].

"Roughness" is an encompassing word that includes many types of landscapes. In inorganic films it can be due to the presence of pores, or the result of island-type of growth, or else be caused by a thermal roughening transition. Even above the melting temperature, capillary waves constitute, in effect, a time-dependent roughness. Perhaps more spectacular is the roughness of films of organic material. For instance, layers of diblock copolymers exhibit at the

interface an archipelago of islands of fixed height[4]. From the scattering point of view, however, roughness can be distinguished by only a few parameters[5]. The lateral extent of the single "bumps," of which roughness is composed, defines the scale of the scattering angles at which scattering can be observed. On the other hand, the height the bumps

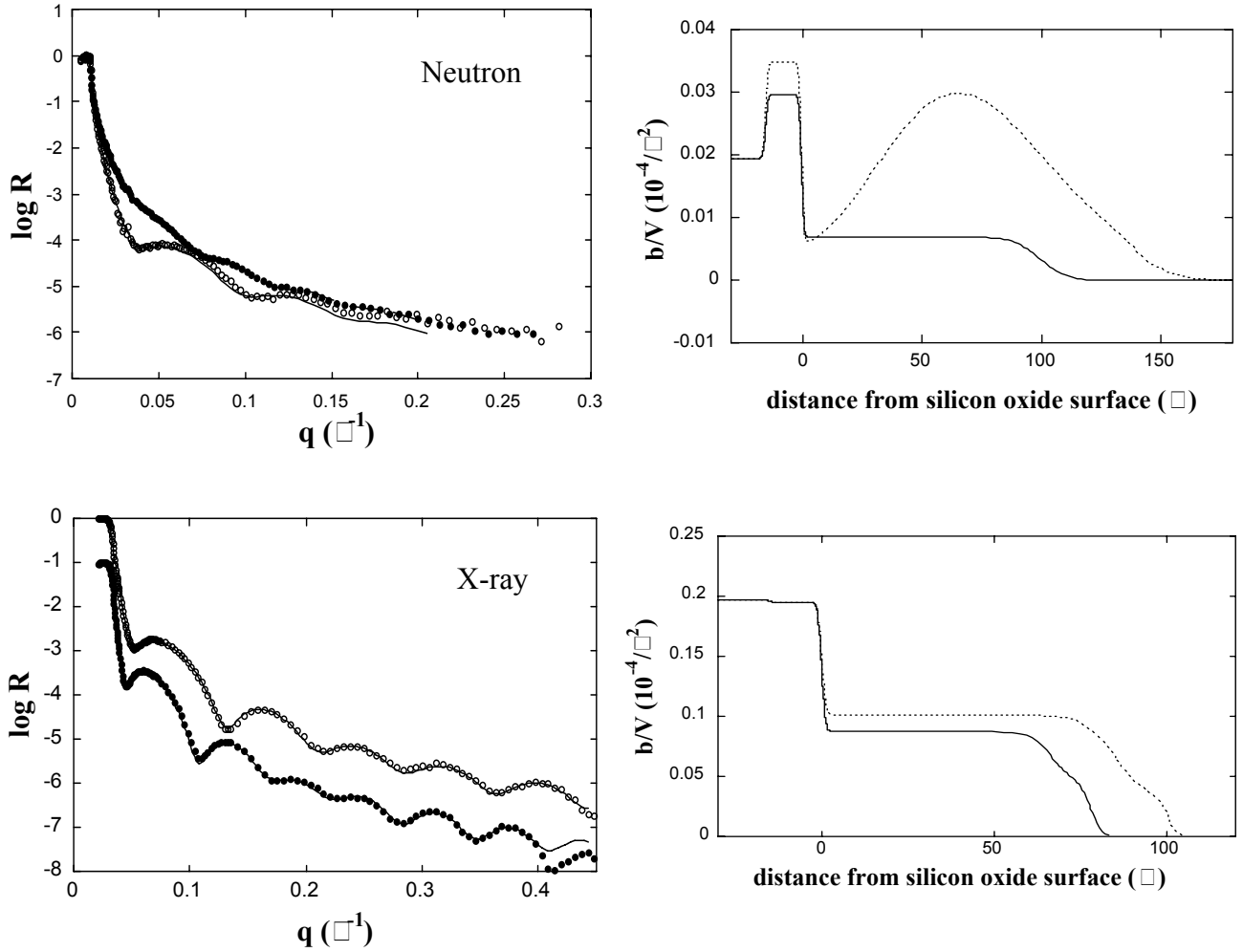

Figure 1: Typical neutron (top) and X-ray (bottom) reflectivity patterns. These were obtained (Ref. 1) from similar films of organosilanes, before (full points) and after solvent swelling (open circles). The brightness of the X-ray source permits to extend the X-ray reflectivity pattern to values of *q* higher than those reachable with neutrons. At the right are scattering amplitude density profiles obtained by least square fitting the reflectivity patterns (continuous line, before swelling; dotted line, after swelling). From these, and the knowledge of the standard scattering amplitude values of elements and isotopes (Refs. 2,3) the chemical density profiles can be obtained. Noticed the contrast obtained in the neutron data by deuterating the solvent.

gives a measure of the amount of scattering-versus the intensity of the specularly reflected beam. These are the main parameters we will be concerned with. Of course from a careful analysis of the scattered intensities detailed features of roughness may be gleaned, such as its fractal dimension, or the extent of lateral correlations, that may reach thousands of Ångstroms.

Fig. 2 shows the geometry of scattering at grazing incidence. The scattered beam is defined by θ_f, the angle with the surface within the reflection plane (as defined by the incident and specularly reflected beams) and φ, the angle off the reflection plane. The relation between momentum transfer and scattering angle within the reflection plane is:

$$q_x = (2\pi/\lambda)(\cos\theta_f \cos\varphi - \cos\theta_i) \sim (\pi/\lambda)(\theta_i^2 - \theta_f^2) \quad (1)$$

while the relation off the reflection plane is:

$$q_y = (2\pi/\lambda)\sin\varphi \cos\theta_f \sim (2\pi/\lambda)\varphi \quad (2)$$

These relations show that for a value of q_x numerically equal to q_y the scattering angles are quite different. For instance, if $q_x = 10^{-4}$ Å^{-1}, the wavelength of the radiation 5 Å and the angle of incidence $\theta_i = 1^o$, the exit angle is 1.28^o. If instead q_y

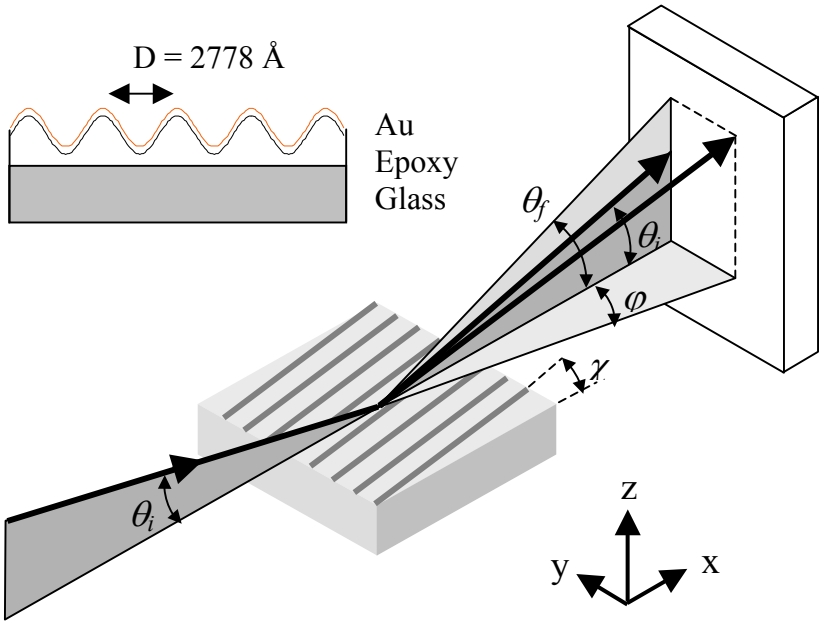

Figure 2: Grazing incidence scattering from a rough surface. The scattering in the plane of reflection (with $\theta_f \neq \theta_i$) is usually referred to as diffuse scattering; that off the reflection plane ($\varphi \neq 0$) as grazing incidence small angle scattering. The scattering object drawn is the holographic optical grating used to provide the proof of principle of the working of SERGIS.

$= 10^{-4}$, $\varphi = 0.005^o$: to distinguish this scattering from the primary beam would require much better angular resolution in the y direction than in the x direction.

2. SCATTERING AT GRAZING INCIDENCE

The difference in the angular divergence caused by q_x, q_y has been well known for over a decade. The in-plane scattering of X-rays was named diffuse scattering at grazing incidence. The off-specular scattering was referred to with the acronym GISAXS, Grazing Incidence Small Angle X-ray Scattering. GISAXS was initially designed to provide size information for islands formed in the initial stages of thin film growth. As pointed in the seminal article by Levine *et al.*[6], the diffuse scattering along q_y, due to height variations in an isotropic x,y surface of the sample is given by [5]:

$$S_{diffuse}(q_y) = (2\pi/q_z^2)\exp(-q_z^2\sigma)\int_0^\infty R \cdot \left[\exp(q_z^2 C(R)) - 1\right] J_0(q_y R) dR \quad (3)$$

where σ is the root-mean-square surface roughness, **R** is the position on the sample surface, and C is the height-height correlation function:

$$C(R) = \langle h(\mathbf{R}')\, h(\mathbf{R}' + \mathbf{R})\rangle \quad (4)$$

Where the bracket indicates the statistical average over pairs of surface points separated by the distance R. The first zero of the Bessel function $J_0(qR)$ occurs at $qR = 2.405$. As a result, if $q > 10^{-2}$ Å^{-1}, then $R < 240$ Å or else Eq. (3) predicts zero or negative intensity. The range of GISAXS is thus clearly defined. A resolution of $q > 10^{-2}$ Å^{-1} is readily obtained in an instrument having a rotating anode as source. Thus GISAXS has been proved to be extremely useful in a variety of experiments (mostly for cases in which the roughness was isotropic) where the lateral dimensions of the roughness "bumps" were sufficiently small. Scanning recent literature, GISAXS has been used to investigate the structure of self-organized Si/SiGe islands[7], the evolution of cluster shape during the growth[8] of Ag on MgO(001), the distribution and shape of self-assembled InAs quantum dots[9] grown on GaAs(001), the structure of 3D-hexagonal mesoporous spin-coated sol-gel films[10] and the morphology of encapsulated iron nanoparticles obtained by co-sputtering and implantation[11].

Using synchrotron radiation, the range of q_y values can be brought to a lower limit of $q_y = 10^{-4}$ Å^{-1}, thereby overlapping considerably the range of q that can be reached in the scattering in the reflection plane. This is achievable basically by tightening the collimation. Neutron sources are less luminous -by several orders of magnitude- than for X-rays, yet the same lower limit has been achieved once, in a major tour de force [12]. We would like to present here a new method, by which values of the momentum transfer as low as $q_y = 10^{-4}$ Å^{-1} can be easily achieved for neutrons, without any sacrifice in intensity: the resolution of the primary beam could be as relaxed as $\Delta q_y = 3 \times 10^{-2}$ Å^{-1}.

3. SPIN-ECHO ENCODING OF SCATTERING

Spin-echo methods have been originally developed to encode the energy transfer of slow neutrons when inelastically scattered by a material[13]. Pynn originally proposed[14] that the Larmor precession of polarized neutrons can be used to encode very small scattering angles without a corresponding angular confinement of the incident beam. Keller[15] and Rekveldt[16] later resumed and expanded these ideas. In particular, Rekveldt designed a small angle scattering[17] instrument based on spin-echo analysis. He also pointed out[18] that a similar scheme could be used in grazing incidence geometry to encode the scattering angle for scattering either in the reflection plane or off the reflection plane. The latter application of spin-echo has truly unique advantages. We will discuss here the principles and the initial tests of the new type of instrument embodying the Spin-Echo Resolved Grazing Incidence Scattering (SERGIS) of slow neutrons.

Fig. 3 gives the conceptual layout of the working of the instrument. Presented here are the two projections of the scattering geometry given in Fig. 2, together with the spin precession devices that enable spin-echo resolution of the angle φ. In the lateral view of the reflection geometry the handling of the neutron spin does not have any role in the

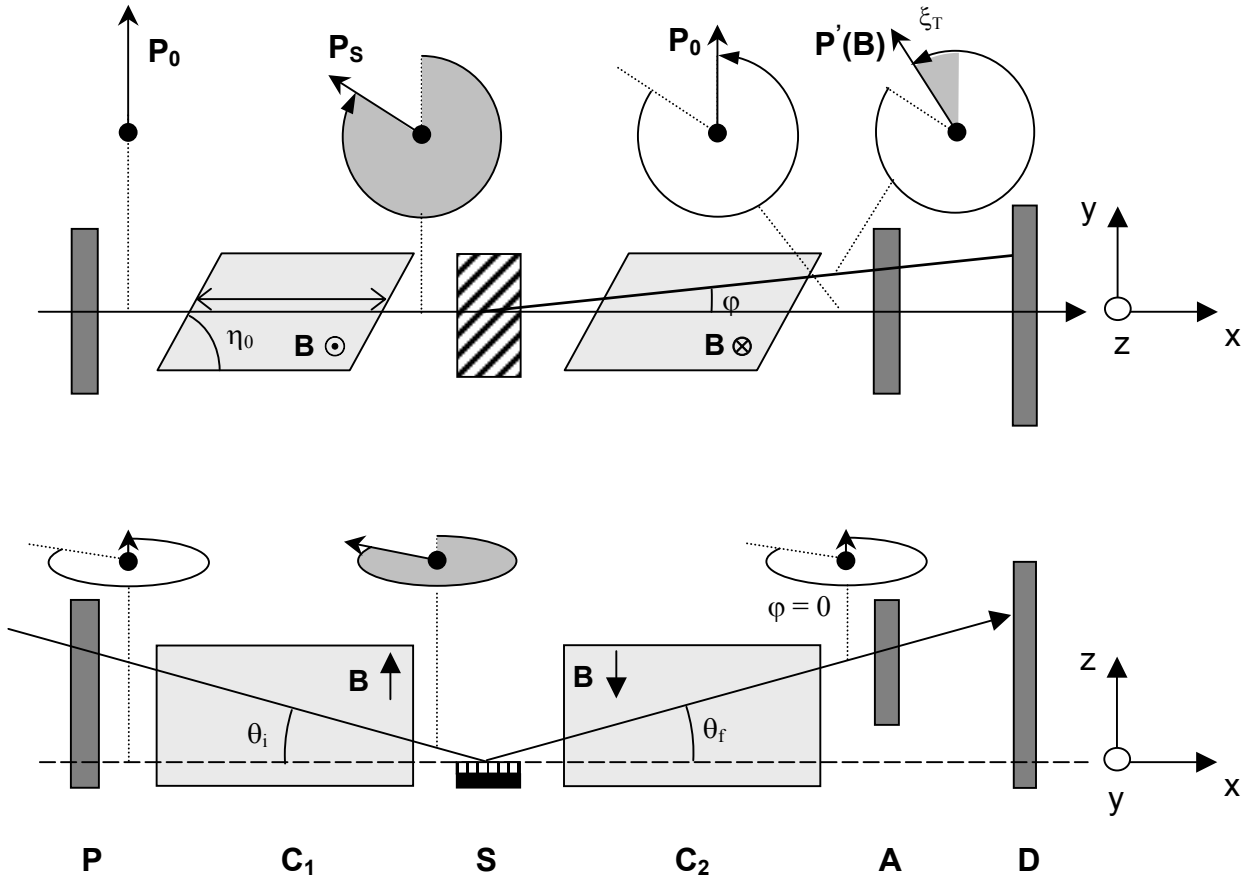

Figure 3: Geometry of SERGIS. Bottom: projected lateral view of the reflection plane. Top: view from above, defining the angle of scattering off the reflection plane, φ. Above each diagram is given the evolution of the neutron spin in the spin-echo circuits before and after scattering.

scattering process, which is assumed to be elastic. Instead, the way in which the scattering angle φ is encoded by spin-echo is visible in the top view of the geometry. The primary beam is polarized at P along the *y* direction before entering the device C_1 (of length *L*), where the neutron spin is brought to rotate in a field *B* applied along *z*. C_1 has rhomboidal shape in the *xy* plane, forming an angle η_0 with the neutron beam, while it is rectangular in the *xz* plane. At the exit of C_1 the neutron spin has a precession angle ξ_1. When the beam is parallel to one of the axis of the rhomboid, the phase of the exiting neutrons after the first precession leg is:

$$\xi = 2\pi\gamma_n BL/v \qquad (5)$$

where $2\pi\gamma_n$ is the gyromagnetic ratio of the neutron ($\gamma_n = 2.92 \times 10^3$ cycles $sec^{-1}Gauss^{-1}$), *B* is magnetic induction field in C_1, *L* the length of the neutron path and *v* the neutron velocity. The neutron is a relatively slow particle - it is equal to 1 Km/sec for λ = 4 Å and is inversely proportional to its wavelength. The neutrons reflected (specularly or not) by the sample S cross a second rhomboid C_2 identical in shape but in a field opposite to that in C_1 For neutrons scattered within the reflection plane (φ = 0) the precession angle in C_2 is $\xi_2 = -\xi_1$: neutrons revert to their original spin state before the entrance of C_1. However, for neutrons scattered by the sample at an angle φ, the precession angle after the second precession leg is [17]:

$$\begin{aligned}\xi_T = \xi_1 - \xi_2 &= 2\pi\gamma_n B(L/v)[1\text{-}1/(1+\sin\varphi\ \mathrm{ctg}\eta_0)] \\ &\sim [2\pi\gamma_n\, BL/v\ \mathrm{ctg}\eta_0]\ \varphi \\ &\cong \{\gamma_n B L/v\lambda\ \mathrm{ctg}\eta_0\}\{2\pi\sin\varphi/\lambda\} = yq_y \end{aligned} \quad (6)$$

The precession angle is given in Eq. (6) in an interesting evolution of representations. The first line is obtained from the straight geometry, for a beam that initially is along the axis of the first precession leg. In the second line, the precession angle ξ_T is shown to be proportional to φ, but with an enhancement factor (in the square bracket) that may well exceed three orders of magnitudes. This is basically the enhancement provided by the spin-echo technique. Such expression is only approximate, becoming less exact with the increase of φ. This also means that the angular divergence of the incoming beam has to be limited - possibly to a divergence of the order of one degree. The last line of Eq. (6) presents, both in an extended and in a compact form, the phase difference in terms of a momentum transfer perpendicular to the reflection plane q_y and of a length y in the same direction. This form is particularly useful for understanding how the precession angle ξ_T is used to extract the physical information.

The polarization of the exiting beam is analyzed at A before reaching the detector. If this is a one-dimensional detector, it records in different channels neutrons scattered at different θ_f angles and integrates over φ. The analyzer A does not give directly the precession angle of the neutron, but rather the projection of the spin on an axis parallel to the axis of the analyzer A, which conventionally has the same orientation of the polarizer P. The polarization of the neutron beam is[17]:

$$p(q_x,q_z,y) = \int S(q_x,q_y,q_z)\cos(yq_y)\mathrm{d}q_y \,/\, \int S(q_x,q_y,q_z)\mathrm{d}q_y \quad (7)$$

From Eqs (3), (4), and (7) it appears that $p(y)$ is basically the normalized correlation function along the y axis. We claim that the span of y bridged by this technique may be brought close to that obtained from scattering measurements along the x direction. For instance it is easy to calculate from Eq. (5) that precession legs of the length L of 40 cm., on which a magnetic field of 2 kOe is applied, cause a precession of 6 Å neutrons equivalent to y = 1.2μm. To verify that this resolution was in fact achievable, we ran a feasibility experiment on an optical diffraction grating.

4. FEASIBILITY TESTS

Feasibility tests were carried on a holographic optical grating[19]. The commercial sample consisted of a polymeric replica of a metallic grating, whose sinusoidally modulated surface had an aspect ratio height/length of the period of 1:3. The polymer base had been covered with an 8000 Å thick layer of gold, with its outer surface conformal to the lower surface. With this thickness only few neutrons with a wavelength of ~ 6 Å are able to penetrate to the substrate, being mostly absorbed in the gold layer. In other words, the sample is not too dissimilar from a semi-infinite layer of gold with sinusoidal surface. The sample's surface was 5 x 5 cm^2.

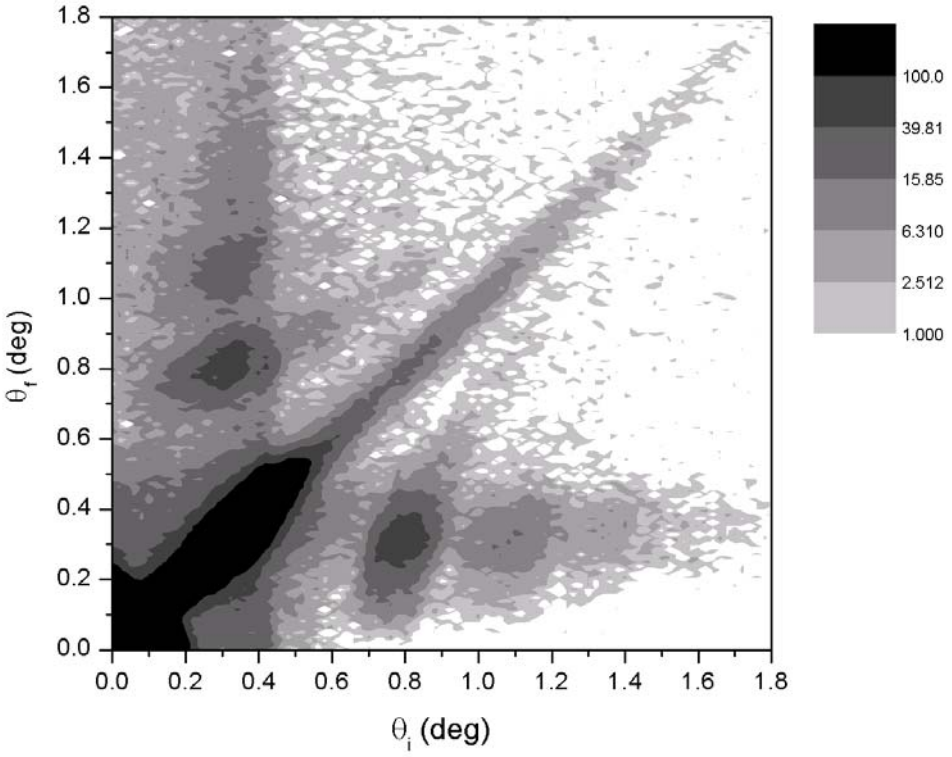

Figure 4: Contour map of the intensities diffracted from an holographic diffraction grating, as obtained at the EVAnescent wave reflecto-diffractrometer at the Institut Laue-Langevin in Grenoble. EVA has a monochromatic neutron beam of 5.5 Å wavelength and a one-dimensional position-sensitive detector that registers the neutrons scattered in the reflection plane over a range of angles θ_f. The 2-dimensional contour plot was obtained by taking measurements at a set of incident angles θ_i. The diagonal streak represents the specularly reflected beam, the sequence of spots to the sides are the diffracted intensities. The holographic grating (Ref. 19) was set at $\chi = 2^o$. In the reflection plane, the period of the diffraction grating appears as $D_{proj} = D/\sin\chi \sim 8\mu m$.

The diffraction pattern from optical gratings of this kind has been previously measured in conventional reflectometers[20,21]. For the present holographic sample, a diffraction pattern from the holographic grating is presented in Fig. 4. This was obtained at the grazing incidence diffractometer EVA at the Institut Laue Langevin in Grenoble for an angle of inclination $\chi = 2^o$ of the grating's grooves with the x axis. Aside from the specular reflection at $\theta_i = \theta_f$ are visible two series of Bragg reflection, at θ_i and θ_f values corresponding (cfr. Eq. (1)) to $q_x = 2n\pi\sin\chi/D$, where D is the grating's period. n is a running integer: even if the grating is sinusoidal, more than one diffraction peak is present. This may seem surprising, because in the first Born approximation an exactly sinusoidal modulation gives rise to a single diffraction peak. In this case, however, the optical transform is not a simple Fourier transform. The surface is described by a sinusoidal function with amplitude of 400 Å. The "roughness" of the surface is large, and cannot be treated in terms of the distorted wave Born approximation (DWBA) as just a first order perturbation from a flat surface. In the well-defined diffraction geometry used the intensities of the harmonics can be calculated - this is the "conical geometry" well studied in the diffraction of electromagnetic waves[22]. The main purpose of the experiment discussed here is to determine the period of the holographic grating with $\chi \sim 0^o$. This is accomplished by spin-echo analyzing the diffracted intensities - that extend to several harmonics.

For an optical grating, $p(y)$ takes a simple form, that is ideal for the demonstration and the testing of the spin echo analysis:

$$S(q_x,q_y,q_z) = C(q_z)\delta[q_x - (2\pi n/D)\cos\chi]\delta[q_y - (2\pi n/D)\cos\chi] \qquad (8)$$

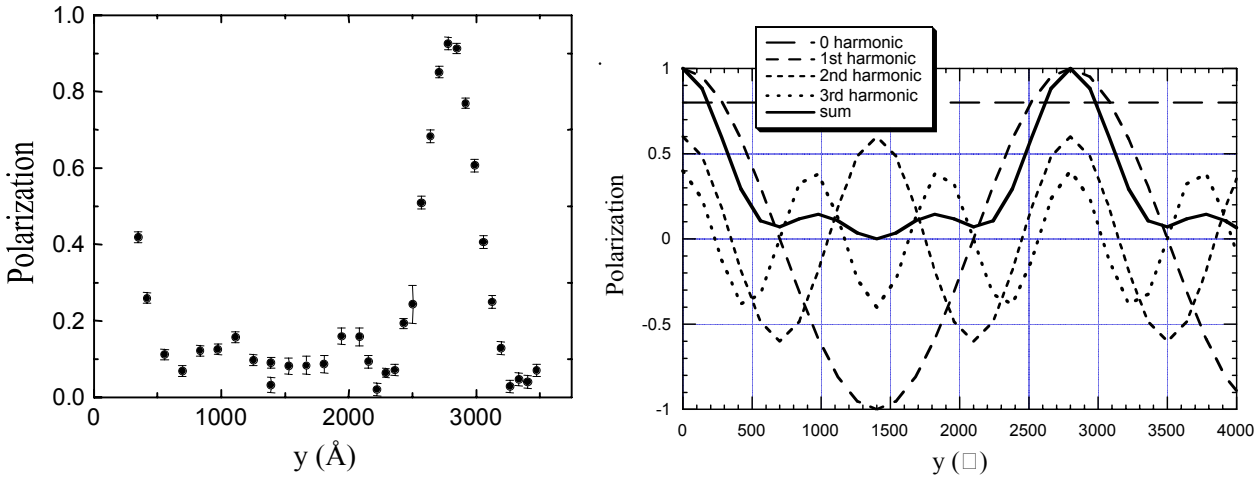

Figure 5: Left: experimental polarization from a D = 2778 Å holographic grating with $\chi = 0^o$. This polarization, measured with a single detector, is the result of a superposition of the polarizations (as selected by the analyzer), weighted with the individual intensities, of all the diffraction lines. Only at a spin-echo length $y = D$ are all of the polarizations equal to 1, resulting in a maximum of the total polarization. The spin echo length y ($= \gamma_n BL/v\lambda \mathrm{ctg}\eta_0$) was varied by sweeping the magnetic field in the spin-echo circuits. Right: simulation of the polarization weighted with the intensity of the individual diffraction lines and their sum as a function of y, for the grating.

From which:

$$p(q_x = 2\pi n/D, y) = \cos[\{\gamma_n BL/v\lambda\ \mathrm{ctg}\eta_0\}(2\pi n/D)\cos\chi] \qquad (9)$$

By sweeping over a range of fields or neutron wavelengths a sinusoidal function should be obtained, whose period is that of the optical grating.

The instrument FLEX at the Hahn-Meitner-Institut in Berlin[23] proved to be ideally suited for the testing of the technical feasibility of the spin-echo experiment, to the point that several of the its features - like the neutron resonance spin echo circuitry - are being adopted in the design of a dedicated SERGIS instrument. FLEX is a three-axis spectrometer installed at a cold neutron guide. The length of the axes (that between monochromator and sample, between sample and analyzer, between analyzer and detector bank) can be varied, as well as their relative angle, in order to optimize the scattering geometry. In the configuration used, the arms before and after the sample were set parallel to each other, and thus FLEX was basically configured as the reflectometer illustrated in Fig. 3. A vertically focusing monochromator provided an incident neutron wavelength of 5.92 Å. The polarizer consisted of a supermirror on silicon substrate, and operated in transmission. After the sample, a similar polarization analyzer operated as well in transmission geometry. The sample's surface was horizontal, and a slit was set in front restricting the illumination on the surface. Slits after the sample prevented the refracted beam from reaching the detector. In the tests discussed here, a single detector collected indiscriminately all the intensities specularly reflected or diffracted from the sample. In a later experiment a two-dimensional, position sensitive detector provided a detailed picture of the reflected and the diffracted beams.

Neutron resonance spin-echo legs, similar to those marked C_1 and C_2 in Fig. 3, were inserted before and after the sample. The principles and operation of the neutron resonance spin-echo circuits have been already discussed in the literature[24]. From a functional point of view, the magnetic field B was identical in both legs and could be simultaneously ramped up to B = 500 Oe. The length of C_1, L_1 = 40cm, was fixed; the length of C_2 was $L_2 = 40\mathrm{cm}+\Delta L_2$, so that L_2 could be adjusted by increments ΔL_2, of fractions of mm, with a micrometer caliper. With the spin-echo circuitry switched on, the polarization for the nth diffraction line is given by a generalization of Eq. (9):

$$P(q_x = 2\pi n/D, yq_y+\phi) = \cos\{(\gamma B/v)[\Delta L_2 + L_0\lambda \mathrm{ctg}\eta_0(2\pi n\cos\chi/D)]\} \qquad (10)$$

The ability to change the effective magnetic field B and the length of the second precession leg L_2 gave an enormous procedural flexibility. Using a constant field B, D can be obtained from the phase shift of the n-th diffraction peak compared to the specular beam. Alternatively, D is obtained by setting $L_1 = L_2$, and then sweeping the neutron polarization as a function of B. The maximum field available and the length of the precession legs restrict the search to gratings whose spacing in the y direction is shorter than 3600 Å. This means that the angle χ has to be kept small, and that only the first period of oscillations is visible on the first ($n = 1$) harmonic.

The D spacing of the grating can be obtained even when a single detector collects the intensity of all n diffracted peaks. As shown in Fig. 5, the polarization of the envelope of diffracted intensities peaks at $y = 2780$ Å, the correct grating's period. At right, a simulation is given of the individual polarizations weighted with the relative intensities of the Bragg reflections that contribute to the envelope. Later measurements with a two-dimensional, position sensitive detector provided the intensity of the Bragg reflections up to the third order. These results are in the process of being analyzed using the algorithm appropriate for conical geometry[22]. However, Fig. 5 already sufficiently illustrate the power of the experimental method: a Bragg reflection - that would have occurred at $\varphi = 0.12^o$ (for $\lambda = 5.92$ Å) has been easily resolved with a beam that in the y direction had a divergence approaching 0.5^o. Yet the instrumental parameters used were far from being at the limit of technology. For instance, the coils generating B were air cooled. If water cooled, the maximum field could have been raised to 2 kOe, providing the capability of measuring grating periods larger than 1 μm.

5. DEVELOPMENT AND APPLICATIONS OF *SERGIS*

The questions that remain to be answered are: what can be done with this new capability, intrinsic of neutron scattering and how does this technique compare with the performance of X-ray scattering? As already discussed, GISAXS has been used for a number of years to measure inclusions and small precipitates on a flat surface or in thin surface layers. Here, the X-ray beam is brought to grazing incidence, at an angle θ_i close to the critical angle, and the intensity scattered at an exit angle θ_f is measured as a function of φ. For X-rays, the high brilliance of the source allows a large range of φ: thus with GISAXS it is possible to determine the size, the correlation and the height of islands a few tens of Å wide and less than 10 Å high. The high brilliance of the source permits also a tightening of the angular resolution sufficient to observe scattering (in φ) from objects as large as 1 μm. Lateral sizes in the range of 10^2-10^4 Å are also in the range of the SERGIS technique while not requiring any tightening of the resolution of the incident beam. Once the possibility of doing these measurements with neutrons is opened, one can exploit fully two great advantages that neutrons offer. The first is the possibility of "coloring" hydrogenous materials with partial deuterium substitution. The second is the small amount of energy that a beam of N neutrons contains compared with a beam of N x-ray photons, and an even smaller probability that this energy be released in the sample. It is worth to examine in more detail two aspects characteristic of this type of scattering.

The advantages of scanning the scattering at grazing incidence in φ rather than θ_f has been already pointed out in the literature[25]. In the distorted wave Born approximation (DWBA) the differential cross section is given by:

$$\frac{\mathrm{d}\sigma}{\mathrm{d}\Omega} = (L_x L_y)(2\pi)^4 (bN)^2 \left|T(\mathbf{k}_i)\right|^2 S(\mathbf{q}') \left|T(\mathbf{k}_f)\right|^2 \qquad (11)$$

where L_x, L_y is the illuminated area of the sample, $T(\mathbf{k})$ is the Fresnel transmission function as a function of incident and scattered momentum $\mathbf{k}_i$ and $\mathbf{k}_f$, respectively. $S(\mathbf{q}')$ is the structure factor, given by Eq. (3), in terms of the momentum transfer in the medium $\mathbf{q}'$. The scattering is caused by the impurity with amplitude b and number density N. Eq. (11) indicates that the scattering function $S(\mathbf{q})$ is modified by the transmission function. The scattered intensity provides an image of $S(\mathbf{q})$ that could be badly distorted, and the transmission function needs to be known with sufficient accuracy in order to recover $S(\mathbf{q})$. To do so, the depth of the scatterer from the surface, its position in the layered material needs to be known in advance. However, T_i and T_f are solely dependent on θ_i and θ_f, i.e. on q_x and q_z. By scanning in q_y (or equivalently in φ), at constant θ_i, θ_f, the transmission functions reduce to multiplying constants and the access to $S(\mathbf{q})$ becomes direct and simple. The simplest form is achieved when k_{iz} and k_{fz} are equal to the critical angle. Then, combining Eqs. (3) and (11):

$$\frac{\mathrm{d}\sigma}{\mathrm{d}\Omega} = (L_x L_y)(4\pi)^4 (bN) 2\pi \int_0^\infty R \cdot C(R) J_0(q_y R) \mathrm{d}R \qquad (12)$$

The experimental cross section - and consequently, the polarization of the exit beam (Eq. (7)) at the critical angle - are closely related to the height-height correlation function.

Up to now we have assumed that the scattering process was entirely elastic. Yet, if inelastic scattering were present, the SERGIS technique would certainly detect them. The effect is most easily seen for a rectangular configuration of the spin-precession legs ($\eta_0 = 0$), a configuration for which spin-echo analysis is insensitive to the scattering angle. In this case Eq. (6) is modified, to give a precession angle:

$$\xi_T \sim [\, \pi \gamma_n BL/v \,]\, \Delta E / E \qquad (13)$$

which shows that the well-known enhancement of the energy transfer which is intrinsic of the spin-echo technique. With the parameters already presented for FLEX, the incident energy is E = 2.3 meV and ΔE = 2.7μeV for $\xi_T = \pi$. Measurements with rectangular spin-precession legs can be used to determine if inelastic effects are present; in the affirmative case, the skewness of the geometry with $\eta_0 = 45^o$ may provide a correlation between energy and momentum transfer. This is a further development of the technique, that requires not only a substantial amount of preparatory analysis, but an identification of the physical phenomena, for which energy exchange takes place within the range observable by the SERGIS technique.

The last, and most important issue is the identification of the systems whose characteristics would be better understood by studying them by SERGIS methods. For bulk samples two techniques can explore the same range of the scattering space. The first one, Spin Echo Small Angle Neutron Scattering (SESANS), which actually stimulated the development of SERGIS, has been tried on only a limited number of samples[17]. The second is ultra-small angle scattering, where the scattered is separated from the incident beam by virtue of an extreme resolution obtained multiple-bounce Bonse-Hart monochromators. On this subject a copious literature has started to appear, dealing with the scattering from large scaled structures, such as those present in sedimentary rocks or colloids or mixtures and blends of polymers[26-28]. SERGIS should be able to observe the same type of phenomena, but in thin films rather than in the bulk. The trend in recent reflectivity measurements[29-31] is towards studying complex polymeric or biological samples, i.e. materials, for which the scattering entities have sizes large in comparison with the nanoclusters that frequently are the objects of study in solid state research. Often bodies of this size cannot be analyzed conveniently or uniquely by direct optical methods, either because they are submerged and not in the topmost layer, or because the identification of their function can be accomplished far better by the selective substitution of light with heavy hydrogen. In all cases, the test of the usefulness of SERGIS can be accomplished only with the collaboration and the involvement of the soft matter and biophysics scientific community.

ACKNOWLEDGMENTS

Work at Argonne was supported by the Department of Energy, Office of Science, under contract 31-109-ENG-38. Work at the MPI Institut in Stuttgart was financed by BMBF under grant 03D05MPG16. The activity of one of us (G.P.F.) was partially supported by the von Humboldt Foundation, during a stage in the Abteilung Dosch of the Max Planck Institut für Metallforschung in Stuttgart. We would like to thank H. Yim and M.T. Rekveldt for providing the artwork on which Figs. 1 and 3 were respectively based.

REFERENCES

1. H. Yim, M.S. Kent, J.S. Hall, J.J. Benkoski and E.J. Kramer, J. Phys. Chem. **B106**, 2474 (2002).
2. G.S. Smith and C.F. Majkrzak, International Tables for Crystallography, Vol. C, P.126, A.J.C. Wilson and E. Prince Eds., Kluwer Academic Publishers, Dordrecht 1999.
3. M. Tolan, X-Ray Scattering from Soft-Matter Thin Films, Springer Tracts in Modern Physics 148, Berlin, 1999.
4. G. Coulon, T.P. Russell, V.R. Deline and P.F. Green, Macromolecules **22**, 2581 (1989).

5. S.K. Sinha, E.B. Sirota, S. Garoff, and H.B. Stanley, Phys. Rev. **B38**, 2297 (1988).
6. J.R. Levine, J.B. Cohen, Y.W. Chung and P. Georgopoulos, J. Appl. Cryst. **22**, 528 (1989).
7. T. Roch, V. Holy, J. Stangl, J. Hoflinger, A. Daniel, G. Bauer, I. Kegel, H. Metzger, J. Zhu, K. Brunner and G. Abstreiter, Phys. Status Solidi **B224**, 241 (2001).
8. A. Barbier, G. Renaud and J. Jupille, Surface Science **454**, 979 (2000).
9. K. Zhang, J. Falta, T. Schmidt, C. Heyn, G. Materlik and W. Hansen, Pure Appl. Chem. **72**, 199 (2000).
10. B.A. Sophie, T. Gacoin, C. Jacquiod, C. Ricolleau, D. Babonneau and J.P. Boilot, J. Mater. Chem. **10**, 1331 (2000).
11. D. Babonneau, A. Naudon, T. Cabioc'h and O. Lyon, J. Appl. Cryst. **33**, 437 (2000).
12. P. Miller-Buschbaum, J.S. Guttmann, M. Stamm, R. Cubitt, S. Cunis, G. von Krosigk, R. Grhrke and W. Petry, Physica B 283, 53 (2000).
13. F. Mezei, Z. Phys. **255**, 146 (1972).
14. R. Pynn, in Neutron spin echo, F. Mezei ed., Lecture notes in physics, Vol 128, Springer, Berlin, 1980.
15. T. Keller, R. Gähler, H. Kunze and R. Golub, Neutron News **6**,16(1995).
16. M. Theo Rekveldt, Nuclear Instr. and Methods **B114**, 366 (1996).
17. M. Theo Rekveldt, Physica **B 276-278**, 55-58 (2000).
18. M. Th. Rekveldt, Physica B **234-236** (1997) 1135.
19. Richardson Grating Laboratory, Catalog 8306Bk-520H.
20. A. E. Munter, S. Adenwalla, G. P. Felcher, X. L. Zhou: Neutron Scattering in Material Science II, eds. D. A. Neumann, Th. P. Russell, B. J. Wuensch, MRS, Pittsburgh, 1995, p. 199.
21. R. M. Richardson, J. R. P. Webster and A. Zarbakhsh: J. Appl. Cryst. **30** (1997) 943.
22. R. Pitit and L.C. Botten, Electromagnetic Theory of Gratings, Advances in Current Physics Series, Vol. 22, Springer Verlag (1980).
23. T. Keller, R. Golub, F. Mezei, R. Gähler, Physica B **241-243** (1998) 101.
24. R. Golub and R. Gähler, Phys. Lett. **A123**, 43 (1987).
25. T. Salditt, T.H. Metzger, J. Peisl, B. Reinker, M. Moske and K. Samwer, Europhysics Lett. 32, 331 (1995).
26. M. Hainbuchner, M. Baron, F. lo Celso, A. Triolo, R. Triolo and H. Rauch, Physica A **304**, 220 (2002).
27. T. Harada, H. Matsuoka, T. Yamamoto, H. Yamaoka, J.S. lin, M. Agamalian and G. Wignall, Colloids and Surfaces A**190**, 17 (2001).
28. M. Agamalian, R.G. Alamo, M.H. Kim, J.D. Londono, L. Mandelkern and G.D. Wignall, Macromolecules **32**, 3093 (1999).
29. G. Fragneto, T. Charitat, F. Graner, K. Mecke, L. Perino-Gallice and E. Bellet-Amalric, Europhysics Lett. **53**, 100 (2001).
30. M. Vogel, C. Münster, W. Fenzl and T. Salditt, Phys. Rev. Lett. **84**, 390 (2000).
31. B.W. Gregory, D. Vaknin, J.D. Gray, B.M. Ocko, T.M. Cotton and W.S. Struve, J. Phys. Chem. B**103**, 502 (1999)

* felcher@anl.gov; phone 1 630 252 5515; fax 1 630 252 7777; Materials Science Division, Argonne National Laboratory, 9700 South Cass Ave, Argonne IL USA 60439.